Rupture Process of the 2020 Caribbean Earthquake along the Oriente Transform Fault, Involving Supershear Rupture and Geometric Complexity of Fault

Tira Tadapansawut[1], Ryo Okuwaki[2,3], Yuji Yagi[2], and Shinji Yamashita[1]

[1]Graduate School of Life and Environmental Sciences, University of Tsukuba, Tsukuba, Ibaraki 305-8572, Japan.
[2]Mountain Science Center, Faculty of Life and Environmental Sciences, University of Tsukuba, Tsukuba, Ibaraki 305-8572, Japan.
[3]COMET, School of Earth and Environmental, University of Leeds LS2 9JT, UK.

Corresponding author: Ryo Okuwaki (rokuwaki@geol.tsukuba.ac.jp)
Second corresponding author: Yuji Yagi (yagi-y@geol.tsukuba.ac.jp)

Key Points:

- We built a kinematic source model of the 2020 Caribbean earthquake to analyze the spatiotemporal evolution of fault geometry and slip
- A fault bend disturbed supershear rupture along the linear fault section and triggered subsequent rupture
- Oceanic transform faults can have geometric complexity that controls rupture evolution

Abstract

A large strike-slip earthquake occurred in the Caribbean Sea on 28 January 2020. We inverted teleseismic P-waveforms from the earthquake to construct a finite-fault model by a new method of inversion that simultaneously resolves the spatiotemporal evolution of fault geometry and slip. The model showed almost unilateral rupture propagation westward from the epicenter along a 300 km section of the Oriente transform fault with two episodes of rupture at speeds exceeding the local shear-wave velocity. Our modeling indicated that the 2020 Caribbean earthquake rupture encountered a bend in the fault system associated with a bathymetric feature near the source region. The geometric complexity of the fault system triggered multiple rupture episodes and a complex rupture evolution. Our analysis of the earthquake revealed complexity of rupture process and fault geometry previously unrecognized for an oceanic transform fault that was thought to be part of a simple linear transform fault system.

Plain Language Summary

On 28 January 2020, a large earthquake occurred on the Oriente fault, an oceanic transform fault in the Caribbean Sea between Jamaica and Cuba. The Oriente fault forms the boundary between the North America and Caribbean tectonic plates. The 2020 Caribbean earthquake was caused by horizontal sliding between the two plates. We used waveforms of the earthquake that were recorded around the world to build a model of the earthquake rupture process. The model showed that rupture during the earthquake was complex, featuring multiple rupture episodes with various rupture speeds and in various directions. Our model suggests that a bend in the fault was responsible for the changes of rupture speed and direction and the triggering of successive rupture episodes. Our analysis of the 2020 Caribbean earthquake has revealed complexity of both fault geometry and rupture process that were previously unknown in oceanic transform fault earthquakes.

1. Introduction

At 19:10:24 UTC on 28 January 2020, a large oceanic earthquake of a moment magnitude (M_w) 7.7 (the 2020 Caribbean earthquake; USGS, 2020) occurred on the Oriente transform fault in the Cayman trough of the Caribbean Sea (e.g., Rojas-Agramonte et al., 2005). Moment tensor solutions determined by the Global Centroid Moment Tensor (GCMT) project (Dziewonski et al., 1981; Ekström et al., 2012) indicate that the 2020 Caribbean earthquake was the result of strike-slip faulting on a vertical fault plane (GCMT, 2020; Fig. 1). A minor tsunami of 0.11 m height was recorded at tide gauges at Port Royal in Jamaica and at Puerto Plata in the Dominican Republic (NOAA, 2020). The aftershock distribution trended roughly west-south-west from the epicenter along the Oriente transform fault; some aftershocks were on the Cayman mid-ocean ridge (Fig. 1).

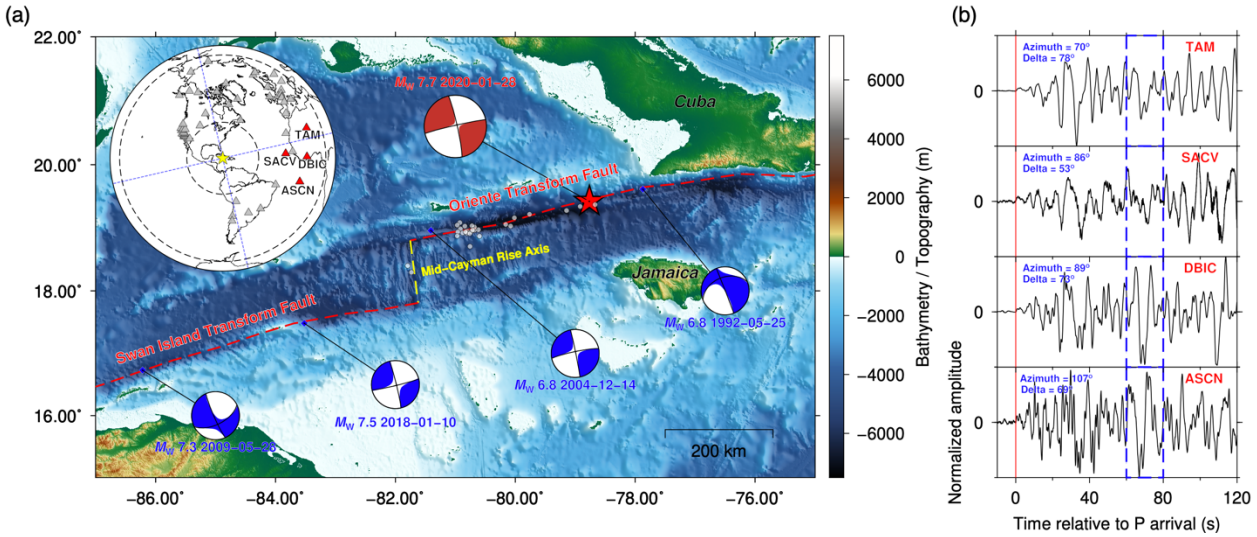

Figure 1. Overview map of the study area, station distribution, and selected waveforms. (a) Focal mechanisms (GCMT, 2020) of the mainshock (red) and previous major earthquakes (blue) are presented as lower-hemisphere stereographic projections. The solid gray circles mark locations of the first week of aftershocks (USGS, 2020). Background topography/bathymetry is from GEBCO (2020). The inset shows the station distribution (triangle) and the epicenter (star) in azimuthal equidistant projection. The circles mark epicentral distances at 30° and 90°. Blue lines represent nodal directions at 77° and 167°. (b) Waveforms from selected stations (red triangles in Fig. 1a). Station codes, azimuthal angles and epicentral distances are also shown. The red line marks the time of the first *P*-wave arrival. Significant amplitude differences noted among stations for later phases lie between the two blue dashed lines.

Oceanic transform faults have been fruitful environments for studies of earthquake-rupture dynamics because of their relatively linear fault geometry and structural heterogeneity (Abercrombie & Ekström, 2001; McGuire et al., 2012; Roland et al., 2012). Despite its apparent linearity of oceanic-transform-fault geometry, some cases of complexity in rupture dynamics have been identified. The 2016 Romanche earthquake is a recent example of complex rupture on an oceanic transform fault, where a long initial rupture phase was followed by a back-propagating supershear rupture (Hicks et al., 2020). Another example is the M_w 7.7 2017 Komandorsky Islands earthquake, where the fault stepover in the transform fault system promoted a supershear transition (Kehoe & Kiser, 2020). Thus, the relationship between the geometric complexity of a fault system and its rupture process is worthy of investigation, even for oceanic transform fault earthquakes.

The source region of the 2020 Caribbean earthquake has been affected by rifting at the mid-ocean ridges along the boundary between the North America and Caribbean plates, which has produced the fracture zone of the Oriente transform fault (e.g., Perfit & Heezen, 1978; Rosencrantz & Sclater, 1986). Near the epicenter, the Oriente transform fault follows a west-south-west-trending seafloor trough, which is 10 km wide, 200 km long, and 6000 to 7500 m deep (Fig. 2a). Farther west, over the last 40 km before the trough reaches the axis of the mid-Cayman rise, it narrows to a width of 2 km (e.g., ten Brink et al., 2002; Hayman et al., 2012; Fig. 2).

Teleseismic waveform data (Fig. 1b) show that the amplitudes of phases recorded 60 to 80 s after the first *P*-wave arrival differ at stations close to the azimuth of one of the nodal directions (77°). This observation indicates that the radiation pattern of seismic energy from the earthquake may not be adequately explained by the single focal mechanism determined by GCMT (2020) and suggests that rupture evolution may have been affected by geometric complexity within the fault system. Thus, the 2020 Caribbean earthquake is a good candidate for investigation of possible complexity of the fault geometry of an oceanic transform fault earthquake and its role in rupture evolution.

In this study we inverted teleseismic waveform data from the 2020 Caribbean earthquake by applying a new method of finite-fault inversion (Shimizu et al., 2020) that represents fault

deformation on an assumed fault by shear-slip vectors by superposition of five basis double-couple components. We showed that the geometric complexity of the Oriente transform fault controlled the multiple rupture episodes and supershear rupture that occurred during the earthquake. Our analysis of the 2020 Caribbean earthquake revealed previously unrecognized source complexity associated with complex fault geometry within an apparently simple oceanic transform fault system.

2. Data and Method

We downloaded vertical component of teleseismic waveform data from 52 stations of the Global Seismographic Network (GSN) and Federation of Digital Seismograph Network (FDSN) through the Incorporated Research Institutions of Seismology (IRIS) Data Management Center. Data were selected to ensure that azimuthal coverage (Fig. 1a) was sufficient to construct a finite-fault model.

To resolve possible changes of fault geometry during rupture propagation, we used the finite-fault inversion method of Shimizu et al. (2020), which can mitigate the effect of modeling errors associated with Green's function uncertainty (Yagi & Fukahata, 2011). This method can flexibly resolve fault geometry by representing the fault-normal and shear-slip vectors (potency density tensors defined by Ampuero & Dahlen, 2005) with five basis double-couple components of moment tensors (Kikuichi & Kanamori, 1991), rather than making an a priori assumption of fault geometry. In the prior constraints of Shimizu et al. (2020), a Gaussian with the same covariance was introduced into the instantaneous spatiotemporal variation of the slip-rate function without distinguishing between the five basis double-couple components. These constraints may, however, have introduced bias because the covariance that determines the smoothness variation for each basis slip component depends on the relative slip rate of each component. In other words, the spatiotemporal slip-rate distributions of the dominant basis components become smoother than those of the minor basis components, which potentially biases the solution and makes it difficult to represent a complex rupture.

To mitigate this bias, we introduced new smoothness constraints by adding the relative standard deviation of each slip component proportional to each basis double-couple component

of the GCMT solution for the 2020 Caribbean earthquake. To avoid instability of the solution due to an extremely small relative standard deviation, we set the relative standard variance of each basis component to be at least 10% of the maximum relative standard deviation. Because the GCMT solution shows dominantly strike-slip faulting, our new formulation takes the standard deviations of the two pure strike-slip components (M1 and M2 of Kikuchi and Kanamori, 1991) to be larger than those of the other slip components (Fig. S10); this enhances the contribution of strike-slip to resolve a possible change of fault geometry, which may have been masked by the artificially dominant dip-slip components in the original method. A comparison of the solutions obtained using our new smoothness constraints with those of the conventional constraints is presented in Figure S11.

We picked *P*-wave first arrivals manually and deconvolved the instrument response to velocity at a sampling interval of 1.0 s. Green's functions were calculated at a sampling interval of 0.1 s by the method of Kikuchi and Kanamori (1991). We used the CRUST2.0 model (Bassin et al., 2000; USGS, 2020) as the near-field velocity structure for calculating Green's functions (Table S1). The sensitivity of the near-field velocity structure was tested by using the CRUST 1.0 model (Laske et al., 2013; Table S2), which showed that our model was insensitive to velocity structure (Fig. S9). We assigned the model fault plane strike and dip angles of 77° and 90°, respectively. The length of the vertical model fault plane was 460 km along strike and it extended to 25 km depth. Sub-faults were 20 km along strike and 5 km along dip. The initial rupture point was placed at 15 km depth at 19.421°N and 78.763°W based on the epicenter determined by USGS (2020). We used a maximum rupture velocity of 6.0 km/s to allow for possible supershear rupture propagation. The slip-rate function for each sub-fault was a linear B-spline function of 61 s duration. Total rupture duration was 100 s. We evaluated the sensitivity of our model to different configurations of our model settings (see Figs. S2 to S9 and Text S1), as discussed in the following sections.

3. Results

Our source model for the 2020 Caribbean earthquake shows strike-slip faulting with almost unilateral westward propagation of rupture from the epicenter (Figs. 2 and 3). The total focal mechanism, which we calculated by integrating all of the potency density tensors (Fig. 2d),

suggests strike-slip faulting with one of the nodal planes striking 258°. The total seismic moment was 0.124×10^{22} Nm (M_w 8.0), which is larger than the USGS W-phase moment tensor solution (USGS, 2020) and the GCMT solution (M_w 7.7). These differences of seismic moment can be explained by our selection of a wider model in both space and time to allow us to cover all possible rupture evolutions, for example, to allow for only minor slip at the western extremity of the Oriente transform fault (Fig. 2a).

We grouped the rupture on the model fault plane into four zones along strike (Fig. 2d) on the basis of the spatial variation of nodal plane distribution extracted from the potency density tensor distribution: –300 to –220 km (zone A), –180 to –130 km (zone B), –120 to –20 km (zone C), and 60 to 100 km (zone D). The strike of maximum potency density changed successively from 78°, to 82°, to 84°, and to 100° from zone A to zone D (Fig. 2a). The changes along strike of the focal mechanism were well resolved, even when we changed the fault geometry and assumed velocity and duration of rupture (Figs. S2 to S9).

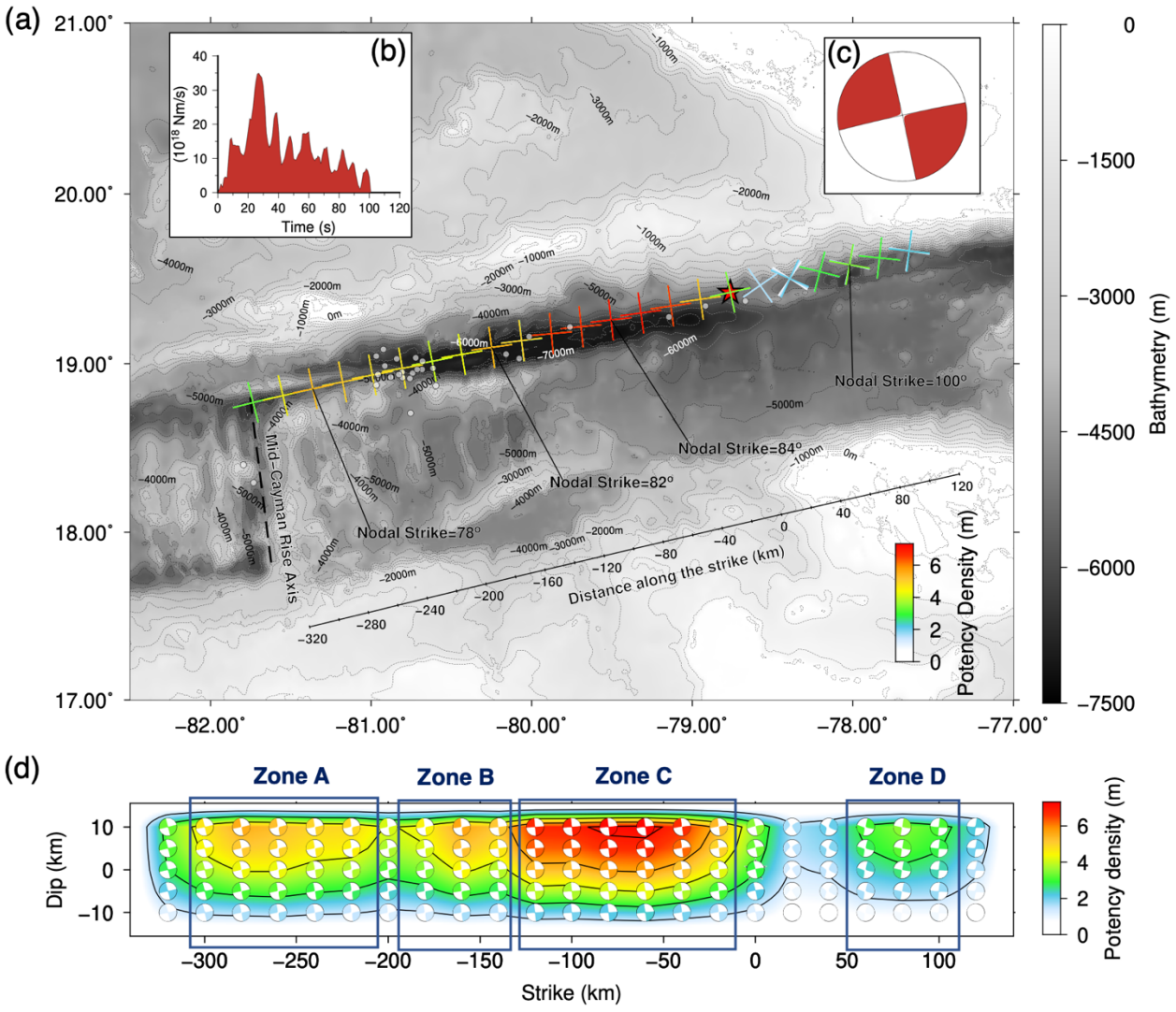

Figure 2. The static distribution of potency density. (a) The map view of static potency density distribution. The nodal planes (cross marker) for each location represent a potency density tensor, calculated by summing all the potency density tensors along the dip direction for each strike direction. All the potency density tensors are shown in Fig. 2d. The gray circle shows the 1-week aftershocks (USGS). The contour represents the bathymetry (GEBCO, 2020). (b) The moment-rate function. (c) The total moment tensor solution estimated from our finite-fault model, using a lower-hemisphere stereographic projection. (d) The cross-section of the static potency density distribution. The focal mechanism is presented by the beach ball at each source knot, plotted using a lower-hemisphere stereographic projection, which are not rotated according to the model-plane geometry (not a view from side but from above).

Snapshots of dynamic slip evolution (Fig. 3) show almost unilateral, relatively high potency-rate density westward rupture propagation from 0 s (rupture nucleation at the hypocenter) to 50 s, followed by lower potency-rate density rupture until 80 s. The initial rupture from 0 to 20 s propagated 80 km west from the epicenter with moderate potency-rate density and was followed by the main rupture episode from 20 to 30 s, about 100 km west of the epicenter, with maximum potency-rate density at 27 s, 80 km west of the epicenter. Fluctuations of potency-rate density between 40 and 80 s indicate several minor sources farther west from the epicenter, until the rupture ceased after 80 s about 300 km west of the epicenter.

The result showed the rupture-front speed was >5 km/s for the initial rupture episode (0 to 20 s; Fig. 3b), which is faster than the local shear-wave velocity (~3 km/s at 15 km depth; Tables S1 and S2). Fast rupture propagation during the initial rupture episode was well reproduced for different assumed maximum rupture velocities (Fig. S2). At the beginning of the main rupture episode (20 to 30 s), the westward propagating rupture front slowed to 2.5 km/s between 20 and 25 s, and then accelerated to >5 km/s after 25 s.

The main rupture episode appears to have expanded both westward and eastward at about 40 s (Fig. 3b), which suggests bilateral rupture involving backward propagation, or a long-retained potency-rate density release of the initial rupture source (0 to –80 km from the epicenter), or both. The spatiotemporal distribution of nodal planes extracted from the modeled potency-rate density tensors shows that their strike varied as the rupture front propagated along the Oriente transform fault (Fig. 3c). From 0 to 20 s, the nodal plane strike was 78°, from 20 to 30 s it rotated clockwise, reaching 83° about 100 km from the epicenter, where the highest potency-rate density was calculated. The strike then rotated counterclockwise to 79° from 45 to 50 s (240 km from the epicenter), which is similar to the strike we obtained near the epicenter (Fig. 3c). The rupture then continued to propagate westward until it reached the western end of the model fault plane.

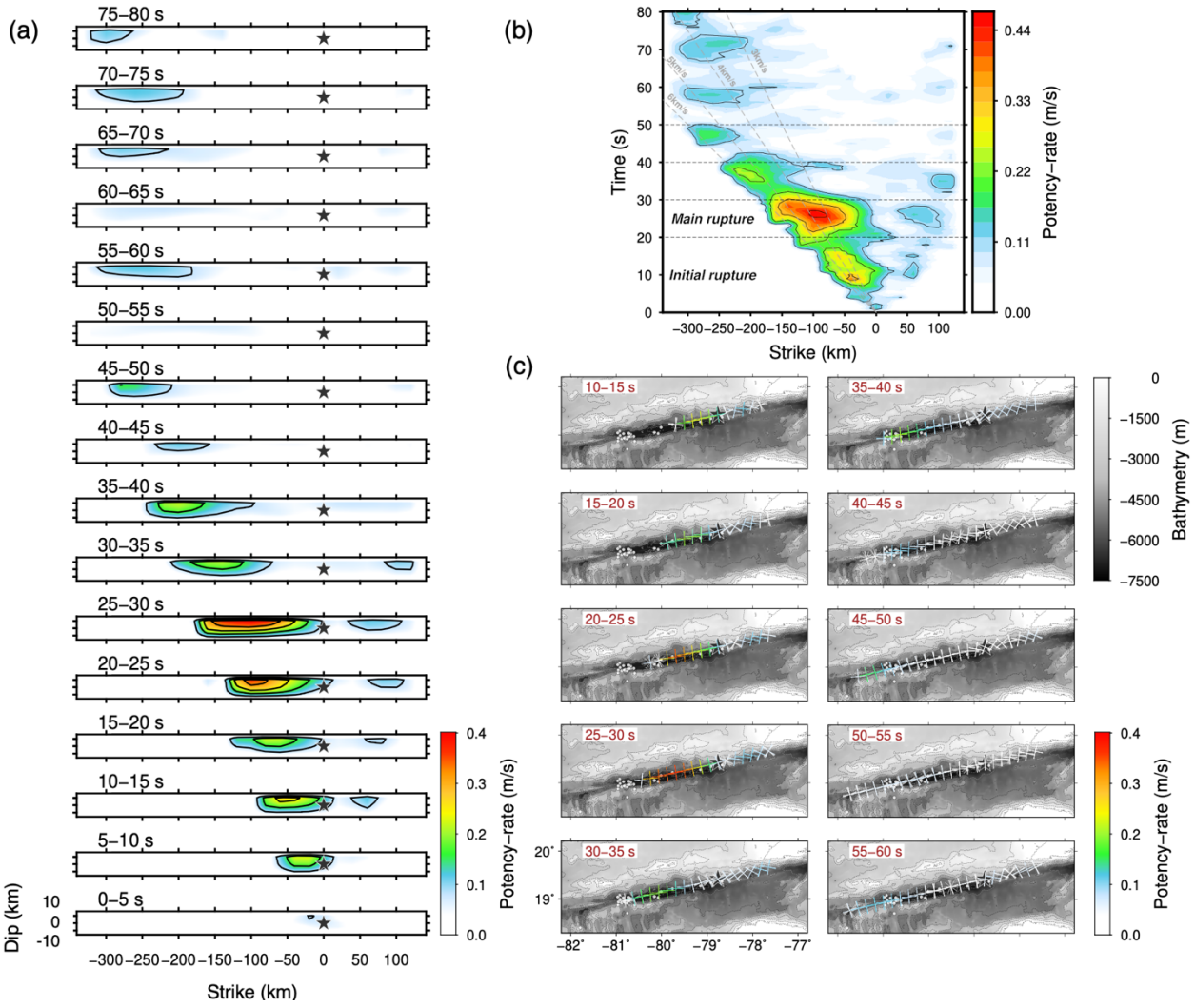

Figure 3. Spatiotemporal distribution of potency-rate density. (a) The snapshots of the rupture propagation. The potency-rate density is averaged within each time window. The star is the hypocenter, and the color contour shows the potency-rate density. (b) The potency-rate density distribution projected along the model strike. The gray dashed lines represent the reference rupture speeds. (c) The map-view snapshots of the averaged potency-rate density within each time window. The cross marker shows the focal mechanism extracted from the resultant potency-rate density tensor. The background contour shows the bathymetry (GEBCO, 2020). The star and gray dot denote the epicenter and the 1-week aftershocks (USGS).

4. Discussion

Our modeling of the spatiotemporal change of fault geometry during the 2020 Caribbean earthquake (Figs. 2 and 3) showed that the strike of the rupture surface deviated from the general strike of the Oriente fault system (77°) in zone C (84°), 80 km west of the epicenter, and then returned to the general strike of the system in Zone A, 280 km west of the epicenter (Fig. 2). These dynamic changes of fault geometry preceded periods of change of potency-rate density. For example, the change of strike that occurred from 20 to 25 s after the hypocentral time followed a period of relatively low potency-rate density (Fig. 3c), whereas the following change from 25 to 30 s was associated with the highest potency-rate density we obtained, which was between 60 and 160 km west of the epicenter. During the period from 40 to 50 s, the strike orientation returned to 78°, which is consistent with the general trend of the western end of the Oriente transform fault (~77°, in accord with the bathymetric feature 240 to 300 km west of the epicenter; Fig. 2a). After this transition of strike, we obtained a moderately high potency-rate density 280 km west of the epicenter. The transitions of fault geometry associated with lower potency-rate density correspond with the area of aftershocks of the 2020 Caribbean earthquake between about 140 and 200 km west of the epicenter (Fig. 2).

Geometrical complexity in earthquake fault, including a fault bend, can affect the fluctuation of rupture propagation (Ulrich et al., 2019, Okuwaki et al., 2020). Simulations of dynamic fault rupture on strike-slip fault systems have demonstrated that an unfavorably oriented fault bend can reduce both the amount of displacement and the rupture speed (Bruhat et al., 2016; Duan & Oglesby, 2005; Kase & Day, 2006). The decrease of rupture speed between the initial and main ruptures (Fig. 3b) might be associated with geometric complexity in the Oriente fault system that prevented smooth rupture propagation and caused a stress change between the areas affected by the initial and main ruptures.

The dominant potency-rate density release we modeled during the main rupture was within zone C, 25 to 30 s after the hypocentral time, after the abovementioned transitions of fault geometry, and corresponds spatially with the location of the deep bathymetric trough (6000 to 7500 m deep; Figs. 2a and 3c) that follows the general trend of the Oriente fault system. After the main rupture, the modeled potency-rate density decreased when it reached the position where the trough narrows abruptly (from 10 to 2 km wide) when it reached the eastern end of zone A.

The western end of zone A is at the mid-Cayman rise axis, where crustal thickness decreases (ten Brink et al., 2002). The deviation of the fault geometry from the general trend of the Oriente transform fault is apparent in our modeling while the rupture follows the wider section of the trough, but to the west, as the rupture traverses the markedly narrower part of the trough and approaches the mid-Cayman rise, the amount of slip decreases and the fault geometry corresponds to the trend of the narrow trough. Thus, our modeling indicates that fault geometry, even that of an oceanic transform fault, can change along strike in response to abrupt changes of the form of bathymetric features, and that these changes may be associated with fracture zones in the upper crust (Roland et al., 2012; van Avendonk et al., 2001).

Our modeling of rupture evolution showed rupture speeds faster than 5 km/s both from 0 to 20 s and from 25 to 40 s after initiation of rupture (Fig. 3b), which is faster than the local shear-wave velocity (~3 km/s at 15 km depth; Table S1). The fast velocity of rupture propagation was well resolved in our modeling, even with different assumed maximum rupture velocities (Fig. S2). Supershear rupture propagation has been identified in other strike-slip earthquakes (e.g., Bao et al., 2019; Bouchon et al., 2010; Kehoe & Kiser, 2020) and has been shown to activate aftershock clusters on secondary ruptures (Bouchon & Karabulut, 2008). Bouchon et al. (2010) reported that smooth fault geometry can promote supershear rupture; in particular, that linear fault geometry around an earthquake epicenter (as is the case for the general trend of the Oriente transform fault) can lead to supershear rupture. Kehoe and Kiser (2020) suggested that a transition to supershear rupture in a fault system can also be associated with complex structural elements such as fault stepovers. Zones of damaged crust along a fault might also be responsible for supershear rupture (e.g., Huang et al., 2016); such zones can be features of a mature oceanic transform fault such as the Oriente transform fault (this study) and the Romanche transform fault (Hicks et al., 2020). However, the speed of westward propagation of the rupture front during the 2020 Caribbean earthquake decreased between 20 and 25 s after the hypocentral time (Fig. 3b) in an area where our modeling showed a change of fault geometry that may have restrained smooth rupture propagation farther west. Alternatively, it is possible that the main rupture of the 2020 Caribbean earthquake did not propagate as a continuation of the initial rupture; rather, it might have been dynamically or statically triggered by the initial rupture. Note that the main rupture is not only a pure unilateral but shows bilateral rupture toward both west and east. The eastern wing of rupture propagating back-toward the epicenter may have broken the region, in which the

rupture was not able to propagate during the initial rupture episode, which may support the hypothesis that the main rupture is rather an individual rupture episode, involving a possible back-propagation of rupture (e.g., Hicks et al., 2020; Idini and Ampuero, 2020).

5. Conclusion

We used a newly developed method of finite-fault inversion to analyze the spatiotemporal evolution of fault geometry and slip during the 2020 Caribbean earthquake on the Oriente transform fault. We modeled successive changes of fault geometry during rupture and these changes controlled a rupture evolution that included a period of supershear rupture. Our study suggests that oceanic transform fault earthquakes, which have previously been thought to have relatively simple fault geometry and source processes, can have complex fault geometry and complex rupture processes associated with distinct bathymetric features.

297 **Acknowledgments**

298 We would like to thank the editor and the reviewers for handing and evaluation of this
299 manuscript. This work has been supported by the Grant-in-Aid for Scientific Research (C)
300 19K04030. The facilities of IRIS Data Services, and specifically the IRIS Data Management
301 Center, were used for access to waveforms, related metadata, and/or derived products used in
302 this study. IRIS Data Services are funded through the Seismological Facilities for the
303 Advancement of Geoscience (SAGE) Award of the National Science Foundation under
304 Cooperative Support Agreement EAR-1851048. Teleseismic waveforms were obtained from the
305 following networks : GEOSCPPE (G;
306 doi:10.18715/GEOSCOPE.G); the Global Seismograph Network (GSN IRIS/IDA, II;
307 https://doi.org/10.7914/SN/II); the Global Seismograph Network (GSN IRIS/USGS, IU;
308 https://doi.org/10.7914/SN/IU); the Canadian National Seismograph Network (CN;
309 https://doi.org/10.7914/SN/CN); the Czech Regional Seismic Network (CZ;
310 https://doi.org/10.7914/SN/CZ); the Netherlands Seismic and Acoustic Network (NL;
311 https://doi.org/10.21944/e970fd34-23b9-3411-b366-e4f72877d2c5); the Mediterranean Very
312 Broadband Seismographic Network (MN; https://doi.org/10.13127/SD/fBBBtDtd6q); the Global
313 Telemetered Seismograph Network (GTSN USAF/USGS, GT; https://doi.org/10.7914/SN/GT);
314 the Southern California Seismic Network (CI; https://doi.org/10.7914/SN/CI); and the Berkeley
315 Digital Seismograph Network (BK; https://doi.org/10.7932/BDSN). We are grateful to to the
316 National Oceanic and Atmospheric Administration (NOAA) for the Tsunami height data. The
317 figures were generated with the Generic Mapping Tools (Wessel et al., 2013, GMT version 5;
318 doi:10.1002/2013EO450001), and the structural velocity models were obtained from the
319 CUST1.0 (Laske et al., 2013) and CRUST2.0 (Bassin et al., 2000).

320

321 **Data Avalability Statement**

322 Waveform data is available via IRIS Data Services (Wilber 3,
323 http://ds.iris.edu/wilber3/find_stations/11176800). The moment tensor solutions are obtained
324 from the GCMT catalog (https://www.globalcmt.org/CMTsearch.html). The Tsunami height is
325 available by the NOAA (https://www.tsunami.gov). The CRSUT 1.0 and CRUST 2.0 structural

velocity models are available through the websites (https://igppweb.ucsd.edu/~gabi/crust1.html) and (https://igppweb.ucsd.edu/~gabi/crust2.html), respectively.

References

Abercrombie, R. E., & Ekström, G. (2001), Earthquake slip on oceanic transform faults. *Nature*, *410*(March), 74–77.

Ampuero, J. P., & Dahlen, F. A. (2005), Ambiguity of the moment tensor. *Bulletin of the Seismological Society of America*, *95*(2), 390–400, https://doi.org/10.1785/0120040103.

Bao, H., Ampuero, J. P., Meng, L., Fielding, E. J., Liang, C., Milliner, C. W. D., Feng, T., Huang, H. (2019), Early and persistent supershear rupture of the 2018 magnitude 7.5 Palu earthquake. *Nature Geoscience*, *12*(March), 200–206, https://doi.org/10.1038/s41561-018-0297-z.

Bassin, C., Laske, G. and Masters, G. (2000), The Current Limits of Resolution for Surface Wave Tomography in North America, EOS Trans AGU, 81, F897.

Bouchon, M., & Karabulut, H. (2008), The aftershock signature of supershear earthquakes. *Science*, *320*(5881), 1323–1325, https://doi.org/10.1126/science.1155030.

Bouchon, M., Karabulut, H., Bouin, M. P., Schmittbuhl, J., Vallée, M., Archuleta, R., Das, S., Renard, F., Marsan, D. (2010), Faulting characteristics of supershear earthquakes. *Tectonophysics*, *493*(3–4), 244–253, https://doi.org/10.1016/j.tecto.2010.06.011.

Bruhat, L., Fang, Z., & Dunham, E. M. (2016), Rupture complexity and the supershear transition on rough faults. *Journal of Geophysical Research*, *121*, 1–15, https://doi.org/10.1002/2015JB012512.

Duan, B., & Oglesby, D. D. (2005), Multicycle dynamics of nonplanar strike-slip faults. *Journal of Geophysical Research*, *110*(December 2004), 1–16, https://doi.org/10.1029/2004JB003298.

Dziewonski, A. M., Chou, T. A., & Woodhouse, J. H. (1981), Determination of earthquake source parameters from waveform data for studies of global and regional seismicity. *Journal of Geophysical Research*, *86*(B4), 2825–2852, https://doi.org/10.1029/JB086iB04p02825.

Ekström, G., Nettles, M., & Dziewoński, A. M. (2012), The global CMT project 2004-2010:

Centroid-moment tensors for 13,017 earthquakes. *Physics of the Earth and Planetary Interiors*, *200–201*, 1–9, https://doi.org/10.1016/j.pepi.2012.04.002.

GCMT. (2020), Mw 7.7 Cuba Region. Retrieved January 28, 2020, from https://www.globalcmt.org/cgi-bin/globalcmt-cgi-bin/CMT5/form?itype=ymd&yr=2020&mo=1&day=28&oyr=1976&omo=1&oday=1&jyr=1976&jday=1&ojyr=1976&ojday=1&otype=nd&nday=1&lmw=7&umw=10&lms=0&ums=10&lmb=0&umb=10&llat=-90&ulat=90&llon=-180&ulon=180&lhd=0&uhd=1000&l.

GEBCO Compilation Group (2020), GEBCO 2020 Grid (Gridded Bathymetry Data Download), doi:10.5285/a29c5465-b138-234d-e053-6c86abc040b9.

Hayman, N. W., Grindlay, N. R., Perfit, M. R., Mann, P., Leroy, S., & De Lépinay, B. M. (2012), Oceanic core complex development at the ultraslow spreading Mid-Cayman Spreading Center. *Geochemistry, Geophysics, Geosystems*, *12*(3), 1–21, https://doi.org/10.1029/2010GC003240.

Hicks, S. P., Okuwaki, R., Steinberg, A., Rychert, C., Abercrombie, R., Bogiaztis, P., Schlaphorst, D., Zahradnik, J., Kendall, J-M., Yagi, Y., Shimizu, K., Sudhaus, H. (2020), Back-propagating super-shear rupture in the 2016 M 7 .1 Romanche transform fault earthquake. *Nature Geoscience (accepted)*, Preprint at https://doi.org/10.31223/osf.io/bs7na.

Huang, M. H., Tung, H., Fielding, E. J., Huang, H. H., Liang, C., Huang, C., & Hu, J. C. (2016), Multiple fault slip triggered above the 2016 Mw 6.4 MeiNong earthquake in Taiwan. *Geophysical Research Letters*, *43*(14), 7459–7467, https://doi.org/10.1002/2016GL069351.

Idini, B., & Ampuero, J. P. (2020), Fault-zone damage promotes pulse-like rupture and rapid-tremor-reversals, Preprint at https://eartharxiv.org/v8xr2/.

Kase, Y., & Day, S. M. (2006), Spontaneous rupture processes on a bending fault. *Geophysical Research Letters*, *33*(10), 1–4, https://doi.org/10.1029/2006GL025870.

Kehoe, H. L., & Kiser, E. D. (2020), Evidence of a Supershear Transition Across a Fault Stepover. *Geophysical Research Letters*, https://doi.org/10.1029/2020GL087400.

Kikuchi, M., & Kanamori, H. (1991), Inversion of Complex Body Waves-III. *Bulletin of the Seismological Society of America*, *81*(6), 2335–2350, https://doi.org/10.1016/0031-9201(86)90048-8.

Laske, G., Masters., G., Ma, Z. and Pasyanos, M. (2013), Update on CRUST1.0 -A 1-degree Global Model of Earth's Crust, Geophys. Res. Abstract, 15, Abstract EGU2013-2658.

McGuire, J. J., Collins, J. A., Gouédard, P., Roland, E., Lizarralde, D., Boettcher, M. S., Behn, M. D., Hilst, R. D. Van Der. (2012), Variations in earthquake rupture properties along the Gofar transform fault , East Pacific Rise. *Nature Geoscience*, *5*(May), 336–341, https://doi.org/10.1038/ngeo1454.

NOAA. (2020), Mw7.7 U.S. Tsunami Warning System, Retrieved January 28, 2020, from https://www.tsunami.gov/events/PHEB/2020/01/28/20028001/5/WECA41/WECA41.txt.

Okuwaki, R., Hirano, S., Yagi, Y., & Shimizu, K. (2020), Inchworm-like source evolution through a geometrically complex fault fueled persistent supershear rupture during the 2018 Palu Indonesia earthquake. *Earth and Planetary Science Letters*, *547*, 116449, https://doi.org/10.1016/j.epsl.2020.116449.

Perfit, M. R., & Heezen, B. C. (1978), The geology and evolution of the Cayman Trench. *Gelogical Society of America Bulletin*, *89*, 1155–1174, https://doi.org/10.1130/0016-7606(1978)89<1155.

Rojas-Agramonte, Y., Neubauer, F., Handler, R., Garcia-Delgado, D. E., Friedl, G., & Delgado-Damas, R. (2005), Variation of palaeostress patterns along the Oriente transform wrench corridor, Cuba: Significance for Neogene-Quaternary tectonics of the Caribbean realm. *Tectonophysics*, *396*, 161–180, https://doi.org/10.1016/j.tecto.2004.11.006.

Roland, E., Lizarralde, D., Mcguire, J. J., & Collins, J. A. (2012), Seismic velocity constraints on the material properties that control earthquake behavior at the Quebrada-Discovery-Gofar transform faults, East Pacific Rise. *Journal of Geophysical Research*, *117*, 1–27, https://doi.org/10.1029/2012JB009422.

Rosencrantz, E., & Sclater, J. G. (1986), Depth and age in the Cayman Trough. *Earth and Planetary Science Letters*, *79*(1–2), 133–144, https://doi.org/10.1016/0012-821X(86)90046-4.

Shimizu, K., Yagi, Y., Okuwaki, R., & Fukahata, Y. (2020), Development of an inversion method to extract information on fault geometry from teleseismic data. *Geophysical Journal International*, *220*(2), 1055–1065, https://doi.org/10.1093/gji/ggz496.

ten Brink, U., Coleman, D. F., & Dillon, W. P. (2002), The nature of the crust under Cayman Trough from gravity. *Marine and Petroleum Geology*, *19*, 971–987.

Ulrich, T., Vater, S., Madden, E. H., Behrens, J., van Dinther, Y., van Zelst, I., Fielding, E. J., Liang, C., Gabriel, A. A. (2019), Coupled, Physics-Based Modeling Reveals Earthquake

418 Displacements are Critical to the 2018 Palu, Sulawesi Tsunami. *Pure and Applied*
419 *Geophysics*, *176*(10), 4069–4109, https://doi.org/10.1007/s00024-019-02290-5.
420 USGS. (2020), M 7.7 - 123km NNW of Lucea, Jamaica. Retrieved January 28, 2020, from
421 https://earthquake.usgs.gov/earthquakes/eventpage/us60007idc/executive.
422 van Avendonk, H. J. A., Harding, A. J., Orcutt, J. A., & McClain, J. S. (2001), Contrast in crustal
423 structure across the Clipperton transform fault from travel time tomography. *Journal of*
424 *Geophysical Research: Solid Earth*, *106*(B6), 10961–10981,
425 https://doi.org/10.1029/2000jb900459.
426 Wessel, P., W.H.F. Smith, R. Scharroo, J. Luis, and F. Wobbe. (2013), Generic Mapping Tools:
427 *Improved Version Release, EOS Trans. AGU*, *94*(45), p.409-
428 410, doi:10.1002/2013EO450001.
429 Yagi, Y., & Fukahata, Y. (2011), Introduction of uncertainty of Green's function into waveform
430 inversion for seismic source processes. *Geophysical Journal International*, *186*(2), 711–720,
431 https://doi.org/10.1111/j.1365-246X.2011.05043.x.
432